Magnetocaloric properties of spheroidal La(Fe,Mn,Si)13Hy granules and their performance in epoxy-bonded active magnetic regenerators

Magnetocaloric properties of spheroidal $La(Fe,Mn,Si)_{13}H_y$ granules and their performance in epoxy-bonded active magnetic regenerators

Bernardo P. Vieira[a], Henrique Neves Bez[a], Michaela Kuepferling[b], Marcelo A. Rosa[a], Deise Schafer[c], Cristiani C. Plá Cid[c], Hugo A. Vieyra[d], Vittorio Basso[b], Jaime A. Lozano[a], Jader R. Barbosa Jr.[a,*]

[a] *Department of Mechanical Engineering, Federal University of Santa Catarina, Florianopolis, SC 88040-900, Brazil*
[b] *Istituto Nazionale di Ricerca Metrologica, Strada delle Cacce 91, 10135 Torino, Italy*
[c] *Department of Physics, Federal University of Santa Catarina, Florianopolis, SC 88040-900, Brazil*
[d] *Vacuumschmelze GmbH & Co. KG, Grüner Weg 37, 63450 Hanau, Germany*

Abstract

Magnetic cooling has been researched as an alternative near room-temperature refrigeration technology for the past two decades. However, one of its greatest limitations is the lack of materials which can be properly shaped for optimal thermal-hydraulic performance while maintaining a substantial magnetocaloric effect at moderate fields (i.e., between 1 and 2 T) and remaining mechanically (and chemically) stable. In this paper, we thoroughly characterized a commercially accessible $La(Fe,Mn,Si)_{13}H_y$ material (available as spheroidal granules), in terms of its magnetocaloric properties and thermal-hydraulic performance in an Active Magnetic Regenerator (AMR) device. The regenerator bed built from epoxy-bonded spheroidal particles endured dozens of hours of operation in AMR cycles without any noticeable degradation of their mechanical integrity, thanks to a comparatively larger $\alpha-$Fe

*Corresponding author
Email address: jrb@polo.ufsc.br (Jader R. Barbosa Jr.)

content and granule porosity. As for the magnetic cooling performance, the AMR has reached a zero-span specific cooling capacity as high as 300 W kg^{-1}. A 1-D two-temperature approach AMR model predicted the AMR performance data with average deviations smaller than 7% for the zero-span specific cooling capacity and 5% for the AMR pressure drop.
Keywords: magnetocaloric effect, first-order material, magnetic refrigeration, regenerator, lanthanum alloys

---

Nomenclature

Roman letters

A	area, m^2
Bi	Biot number
c	specific heat capacity, J kg^{-1} K^{-1}
c_{E}	Ergun constant
$D_{\|\|}$	longitudinal thermal dispersion constant, m^2 s^{-1}
d	diameter, m
e	thickness, m
f	cycle frequency, Hz
Fo	Fourier number
H	magnetic field, T
h	convection heat transfer coefficient, W m^{-2} K^{-1}
K	porous medium permeability, m^2
k	thermal conductivity, W m^{-1} K^{-1}
L	length, m
M	magnetization, A m^{-1}
m	mass, kg

Nu	Nusselt number
P	pressure, Pa
Pe	Peclet number
Pr	Prandtl number
p	perimeter, m
$\dot{Q}$	heat exchange rate, W
$\dot{q}$	energy rate per unit volume, W m^{-3}
R	magnetic circuit radius, m
R	thermal resistance, K W^{-1}
Re	Reynolds number
S	entropy, J K^{-1}
s	specific entropy, J kg^{-1} K^{-1}
T	temperature, K
t	time, s
u	Darcy velocity, m s^{-1}
V	Volume, m^3
y	position perpendicular to the regenerator length, m
z	position along the regenerator length, m

Greek letters

α	thermal diffusivity, m^2 s^{-1}
β	interstitial surface area density of the pores, m^{-1}
ΔT	temperature difference, K
ε	volume fraction (porosity)
μ	dynamic viscosity, kg m^{-1} s^{-1}
μ_0	vacuum magnetic permeability, 4π x 10^{-7} N A^{-2}
ρ	density, kg m^{-3}

τ	period, s
φ	weight fraction
ω	angular speed, rad s^{-1}

Sub and Super-Scripts

ad	adiabatic
air	air
apl	applied
c	cross section
C	Curie
cold	cold source
cond	conduction
conv	convection
csg	casing
dp	particle diameter
eff	effective
ep	epoxy
eq	equivalent
f	fluid phase
hot	hot source
MCE	magnetocaloric effect
MCM	magnetocaloric material
p	particle
pm	porous medium
reg	regenerator
s	solid phase

wall casing wall

1. Introduction

Research in magnetic refrigeration and other caloric cooling technologies has increased exponentially in the past decades [1, 2, 3, 4], indicating that alternative technologies could displace conventional vapor compression coolers in some applications in the future if issues related to efficiency, production and material costs are solved [5, 6].

The Magnetocaloric Effect (MCE) is the thermal response of a magnetic material when subjected to a changing magnetic field. It is more significant in the vicinity of the magnetic transition temperature, i.e., the Curie temperature, T_C. For most materials and alloys intended for cooling and heat pumping at near room temperature, typical values of the adiabatic temperature change, ΔT_{ad}, at the Curie temperature range from 2 to 8 K, for an external magnetic field change of 2 T [7, 8]. For materials with a Second-Order Phase Transition (SOPT), the temperature range around T_C over which ΔT_{ad} is significant is of the order of 30 K. On the other hand, First-Order Phase Transition (FOPT) materials exhibit comparatively larger isothermal entropy changes over narrower temperature ranges around T_C, and adiabatic temperature changes of the order of 10 K for a field change of 2 T [1, 9]. FOPT materials usually exhibit a structure/volume change across the phase transition which, when cycled in magnetization/demagnetization loops, can lead to fatigue [10]. Moreover, FOPT materials may also exhibit hysteresis, which results in energy loss and thermal inefficiency [11, 12].

A wide variety of FOPT alloys have been investigated aiming at their application in magnetic heat pumping, e.g., Gd-Si-Ge [13], Mn-As [14], Fe_2-P

[15], Heusler alloys [16, 17] and La(Fe,Co,Si)$_{13}$ [18, 19]. However, these materials present one or more of the following problems: critical/expensive elements, large hysteresis, short fatigue life, and insufficient magnetocaloric effect. Among the FOPT magnetocaloric materials (MCMs), two alloys, Fe_2P and La-Fe-Si, have been produced for commercial purposes (although only the latter is currently commercially available) Rev3C1. As most FOPT materials are brittle, one should expect spheroidal particles to have longer fatigue life than irregular ones due to lower quantities of stress concentration features, such as sharp corners. However, different fabrication routes are needed to process irregular and spheroidal particles, and this may result in different magnetocaloric properties.

In order to increase the effective temperature change associated with the material and enable larger temperature spans, thermal regeneration cycles are used [20, 21]. In the Active Magnetic Regenerator (AMR), the magnetocaloric material comprises a porous medium subjected to alternating (hot and cold) fluid blows in synchrony with magnetic field changes [21, 22]. A somewhat recent approach has been to layer several magnetocaloric materials along the regenerator bed so as to develop cascading magnetic transition temperatures, assuring that each layer would work around the peak of the magnetocaloric effect [23, 24]. Apart from their effect on the system operating parameters (frequency, utilization, temperature span), the number of regenerator layers will change according to the type of magnetic phase transition exhibited by the magnetocaloric material, i.e., FOPT or SOPT. Altogether, the number of studies on multilayer AMRs composed of La-Fe-Si alloys is much larger than for any other material [25, 26, 27, 28]. In some of those studies, epoxy bonding has been used to mitigate the effects of the magneto-structural transitions present in those alloys, which cause

a reduction of the mechanical strength of the matrix. Nevertheless, only recently issues related to thermo-mechanical reliability (and functional stability) of the AMR have received more attention [29, 30, 31]. In Ref. [29], an AMR made from parallel plates of epoxy-bonded La-Fe-Co-Si alloys with an hydraulic diameter of 0.2 mm operated for more than 90,000 cycles in magnetic field changes of 1.15 T. A 10-K no-load temperature span was reported. Ref. [30] carried out passive regenerator tests to compare the thermal-hydraulic performances of epoxy-bonded regenerators made from irregular (i.e., sharp edged) and nearly spherical $La(Fe,Mn,Si)_{13}H_y$ granules. An AMR with five layers of $La(Fe,Mn,Si)_{13}H_y$ (made from spheroidal particles) achieved a no-load temperature span of approximately 17 K. The results agreed well with an exisiting 1-D AMR model.

The present study spans all the research related steps of the development of $La(Fe,Mn,Si)_{13}H_y$ AMRs, covering the areas of material synthesis, property measurement, AMR testing and modelling. In the first part, an extensive characterization of the magnetocaloric properties of three commercially available $La(Fe,Mn,Si)_{13}H_y$ alloys shaped as quasi-spherical granules, with Curie temperatures of 282.9, 296.9 and 303.5 K, is carried out. The analysis is followed by an experimental assessment of the thermal-hydraulic performance of a three-layer AMR formed by $La(Fe,Mn,Si)_{13}H_y$ granules of different compositions (corresponding to Curie temperatures of 299.9, 303.5 and 307 K). In the AMR test, the regenerator endured dozens of hours of cyclic operation without any noticeable mechanical deterioration, which can be attributed to a large $\alpha-$Fe and material porosity content. The experimental results for the AMR temperature span, pressure drop and cooling capacity were compared with a one-dimensional two-temperature porous medium AMR model, which took into account the influence of the epoxy bonding on

the thermal-hydraulic performance of the regenerator. The model showed a good agreement, with average deviations lower than 5% and 7% for the average regenerator pressure drop and zero-span specific cooling capacity, respectively. These results are discussed in the light of the trade-offs involving mechanical stability and the refrigerating effect associated with the larger $\alpha-$Fe content in the magnetocaloric refrigerant.

2. Magnetocaloric Materials

2.1. Synthesis and Characterization

The La(Fe,Mn,Si)$_{13}$H$_y$ spheroidal particles were produced by a process described in Ref. [32]. Feedstocks made of powder blends and a binder were extruded in a 12-mm twin screw extruder using a die with a circular cross section. The extrudates were cut and spheronized to produce the spheroidal particles. Scanning Electron Microscope (SEM) images of the particles are shown in Fig. 1. The binder was thermally debinded between 573 K and 773 K and then sintered around 1373 K. The particles were finally hydrogenated as described in Ref. [33] in order to adjust their transition temperatures around room temperature. The nominal compositions of the particles produced in the present study are presented in Table 1. The hydrogen content has not been recorded.

It should be mentioned that, although five samples with distinct material compositions were produced as part of this study — and were preliminary characterized at Vacuumschmelze GmbH & Co. (Hanau, Germany) to determine their Curie temperatures — due to logistical issues, only three samples were fully characterized for their calorimetric properties and the amount of $\alpha-$Fe at INRiM (Turin, Italy) and UFSC (Florianopolis, Brazil). Rev4C4a

Table 1: Nominal compositions and Curie temperatures of the particles synthesized as part of this study.

Composition	**Temperature**
$LaFe_{11.13}Mn_{0.51}Si_{1.36}$	282.9 K
$LaFe_{11.2}Mn_{0.42}Si_{1.38}$	296.9 K
$LaFe_{11.23}Mn_{0.4}Si_{1.38}$	299.9 K
$LaFe_{11.31}Mn_{0.35}Si_{1.33}$	303.5 K
$LaFe_{11.34}Mn_{0.32}Si_{1.33}$	307.0 K

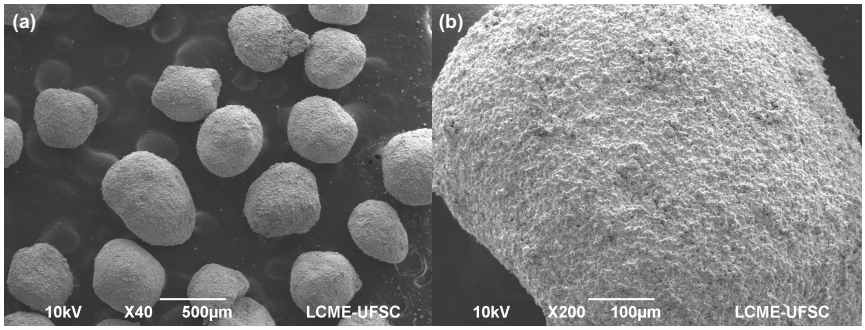

Figure 1: SEM images of the spheroidal $La(Fe,Mn,Si)_{13}H_y$ particles. Although some particles are nearly spherical, others have an approximately cylindrical shape as a result of the production process (Fig.a). The particles are highly porous at the surface (Fig.b), which helps to explain their comparatively higher mechanical stability.

Calorimetric measurements were carried out in a custom-built Peltier Differential Scanning Calorimeter (DSC) under a magnetic field [34]. The DSC chamber was filled with argon gas at 1.1 atm and calibrated with sapphire at the same conditions of the experiments. The masses of the samples were in the range of 45 mg. The thermal contact resistance between the sample and the Peltier module was computed by carrying out measurements at two different rates (50 and 100 mK s^{-1}). This allows an accurate detection of

dynamic features, such as temperature hysteresis, since the thermal contact resistance introduces a time constant. In fact, by considering the thermal resistance, the uncertainty of the temperature measurement was ± 0.2 K. By considering the thermal resistance as described in Ref. [35], rate independent heat capacity curves were successfully obtained at different magnetic fields. Measurements were carried out in both cooling down and heating up modes to quantify any thermal hysteresis.

Back-Scattered Electron (BSE) images taken with a scanning electron microscope (JEOL JSM-6701F) are shown in Figure 2. In the zoomed-in image (Figure 2.b), it is possible to observe the presence of three distinct chemical phases in the material. From the characterization of these phases by Energy Dispersion Spectrometry (EDS), it can be concluded that the dark gray region corresponds to the $\alpha-$Fe phase. The analysis of images of this type revealed an amount of $\alpha-$Fe of about 20 vol.% in the material. X-Ray Diffraction (XRD) was performed on the spheroidal particles in a Rigaku Miniflex II difractometer. Using the Rietveld method, an amount of $\alpha-$Fe of about 14 wt.% was calculated and the refinement is shown in Figure 3. The arrows show unrefined peaks, which may indicate the presence of a La-rich phase, as observed in the BSE image in Figure 2(b) (white colored phase). Additional measurements using a Vibrating Sample Magnetometer (VSM) indicated an amount of $\alpha-$Fe of about 13.5 wt.%, confirming the previous results.

The higher $\alpha-$Fe fractions were obtained through variations in the debinding step which lowered the sintering activity, thus also influencing the somewhat larger particle porosity. Such effects were not accidentally obtained, since there was an interest in producing more mechanically stable particles and exploring the trade-off between mechanical and thermody-

namic properties, which are known to decrease with the presence of $\alpha-$Fe. Potential disadvantages of real devices that use a more (mechanically) stable material at the expense of a lower magnetocaloric effect are related to the size of the system components (magnetic circuit, pumps, motors and the AMR itself) which must be larger to compensate for the reduction of the refrigerating effect. However, a system-level analysis of such drawbacks is outside the scope of the present paper. Rev3C2, Rev4C1, Rev4C4b

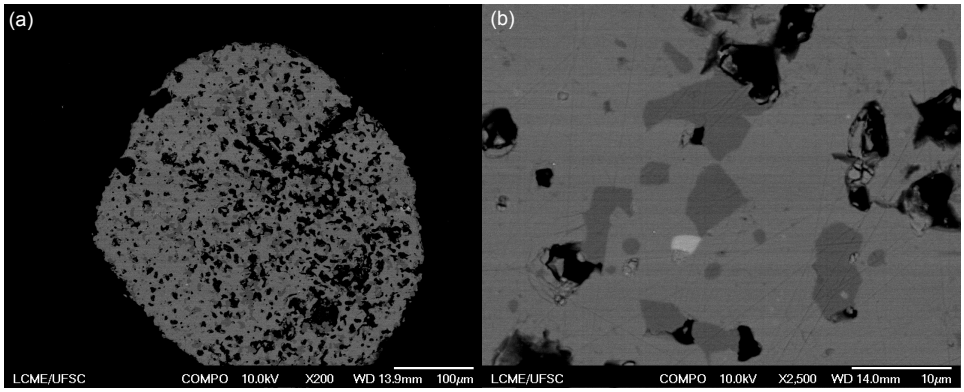

Figure 2: (a) BSE image of a spheroidal particle showing a large porosity. (b) Zoomed-in image: The black region within the sphere is a pore, the darker gray region is $\alpha-$Fe, the lighter gray region is the magnetocaloric phase, and the white region is La-rich phase.

2.2. Magnetocaloric Properties

Figure 4 shows the experimental specific heat capacity curves at different applied magnetic fields. The labels on each set of curves correspond to the nominal Curie temperature of each particular alloy (loose particles), in K. Moreover, the dashed and solid lines indicate cooling down and heating up modes, respectively. Table 2 summarizes the properties and parameters derived from the c_s measurements reported in Fig. 4. Here, T_C is defined as the temperature at the peak of c_s during the heating procedure at 0 T.

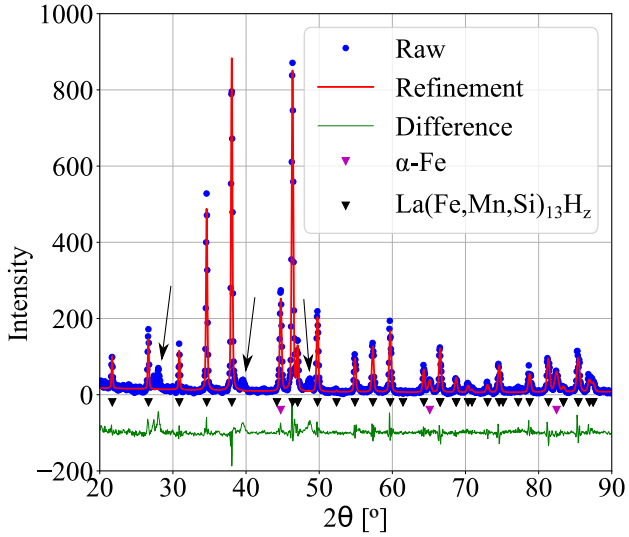

Figure 3: (color online) XRD pattern and Rietveld refinement of the spheroidal particles showing two phases accounted in the refinement. The arrows show peaks not refined.

ΔT_{hyst} is the transition temperature hysteresis and $\mathrm{d}T_{\mathrm{C}}/\mathrm{d}H$ is the shift of the transition temperature as a function of the field; both quantities were calculated fitting first-order polynomials to the temperatures at the peak values of c_{s} for each alloy.

It becomes clear from the specific heat capacity data that the spheroidal particl~~not exhibit thermal hysteresis~~, ΔT_{hyst}, which is often an important source of energy losses in AMRs. This represents a significant improvement when compared to previously characterized irregular shaped particles of similar composition [35]. Indeed, another practical problem with ΔT_{hyst} related to modelling of AMRs is how to efficiently incorporate such an effect in the model. Therefore, the lack of hysteresis is a clear advantage of the present material. Finally, $\mathrm{d}T_{\mathrm{C}}/\mathrm{d}H$ was observed to follow the same trend of the irregular La(Fe,Mn,Si)$_{13}$H$_y$ particles characterized in Ref. [35],

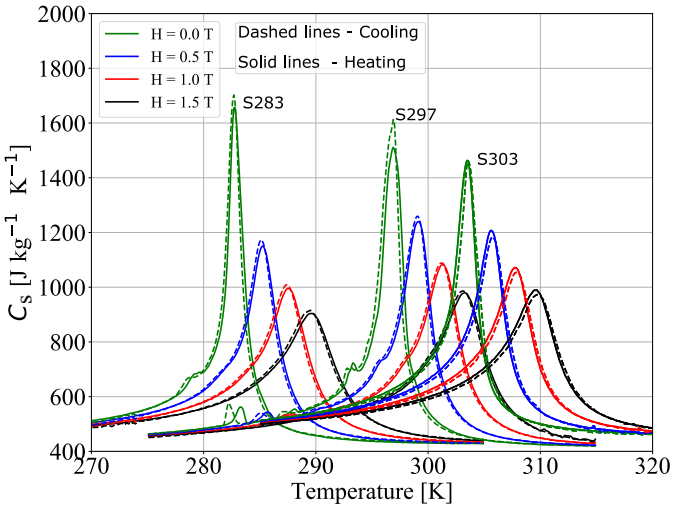

Figure 4: (color online) Specific heat capacity as a function of temperature for different applied magnetic fields for the spheroidal La(Fe,Mn,Si)$_{13}$H$_y$particles. Dashed lines indicate cooling down mode, while solid lines indicate heating up mode.

i.e., both decrease with an increase in T_C. From the Clausi uation, which indicates the first-order contribution to the entropy change:

$$\Delta S = -\Delta M \left(\frac{\mathrm{d}T_C}{\mathrm{d}H}\right)^{-1} \quad (1)$$

one would expect that as T_C increases for the different alloys, the first order contribution to the entropy change would also increase, because $\mathrm{d}T_C/\mathrm{d}H$ decreases with temperature [36]. Nonetheless, this is not so trivial for the present spheroidal particles. Although $\mathrm{d}T_C/\mathrm{d}H$ shows a clear trend, i.e., that of an increasingly first-order charact th an increase in T_C, neither ΔT_{hyst} nor ΔS and ΔT_{ad} follow this tendency; those properties remain somewhat constant is could be related to the large $\alpha-$Fe content seen in Figs. 2 and 3, which is an indication that not all of the Fe added during the fabrication process has been incorporated into the magnetocaloric

phase. This results in a substantial chemical inhomogeneity in the desired phase, which can lead to less obvious FOPT features, as demonstrated elsewhere [37].

Table 2: General properties of the spheroidal (loose) particles. The expanded uncertainty of the measured temperatures are ± 0.2 K. The values of T_{C}, $\Delta S^{\max}$ and $\Delta T_{\mathrm{ad}}^{\max}$ are taken from the heating procedure.

ID	T_{C} [K]	ΔT_{hyst} (0 T) [K]	dT_{C}/dH [K T $^{-1}$]	$\Delta s^{\max}$ ΔH =1.5 T) [J kg^{-1} K^{-1}]	$\Delta T_{\mathrm{ad}}^{\max}$ ΔH =1.5 T) [K]
S283	282.8	0.0	4.51	10.04	3.99
S297	296.9	0.0	4.26	10.10	4.00
S303	303.5	0.0	4.14	9.24	3.60

Figure 5 presents the calculated magnetocaloric properties of the spheroidal La(Fe,Mn,Si)$_{13}$H$_y$ particles made from the different alloys. Again, there is clearly a negligible hysteresis associated with the properties of the spheroidal particles. However, compared with previously assessed irregular shaped La(Fe,Mn,Si)$_{13}$H$_y$ particles [35], the spheroidal particles exhibit lower magnitudes and less sharp peaks. Again, this may be connected to the fact that the spheroidal particles have a much higher $\alpha-$Fe content and a higher porosity than the irregular particles, which is responsible for a decrease of the magnetocaloric effect. On the other hand, the higher $\alpha-$Fe content improves the mechanical integrity and fatigue life as described by [10, 38].

It is well documented that the La(Fe,Mn,Si)$_{13}$H$_y$ family with low Si and Mn content exhibits a large volume change around the phase transition, of about 1 % [39], which can lead to significant strain [40] and, consequently, high internal stresses. Therefore, cycling such materials around the transi-

tion temperature, which will certainly occur in AMRs, may cause fatigue. The material internal porosity works in two different ways to increase the fatigue life: it helps to absorb some of the volume change, and halts the propagation of cracks when they reach a critical size. Moreover, the spheroidal particles are much less susceptible to the appearance of stress concentration points on the surface, which is a major issue in irregular particles. In sum, one expects that the issue of short fatigue life typical of FOPT magnetocaloric materials can be appropriately dealt with in the current scenario with the use of spheroidal particles.

3. Experimental Work

3.1. Active Magnetic Regenerator

The three-layer regenerator was assembled using different batches of spheroidal La(Fe,Mn,Si)$_{13}$H$_y$ particles (fabricated by the same team through the above described processes), all with a mean diameter of 700 μm. As with the loose particles analysed in Section 2, the average particle size was aimed to be 515 μm with sieved particles between 400 and 630 μm. However, due to variations in the extrusion process, it was not possible to produce perfectly spherical particles. As a result, somewhat elongated particles were also produced with length-to-diameter aspect ratios larger than unity, effectively shifting the average particle size. Rev3C3

The Curie temperatures of the materials assembled in the regenerator were 299.9, 303.5 and 307 K (see Table 1). It should be mentioned that a FOPT regenerator with three layers and a difference between the highest and lowest Curie temperatures of $\sim$7 K has a somewhat limited range of applicability in real cooling devices. However, this simpler configuration not

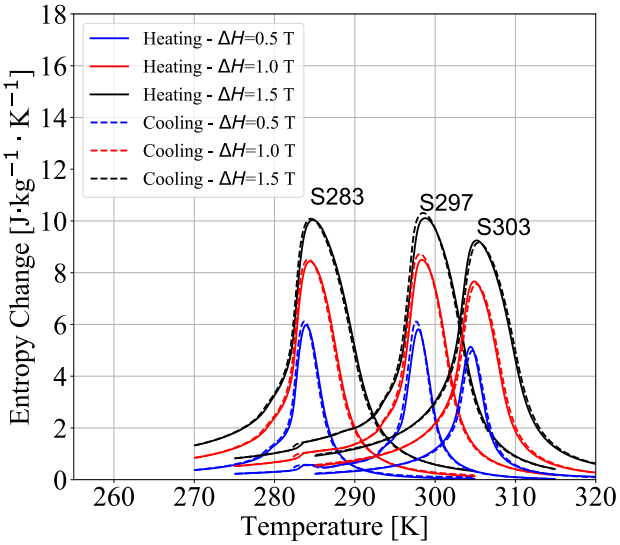

(a)

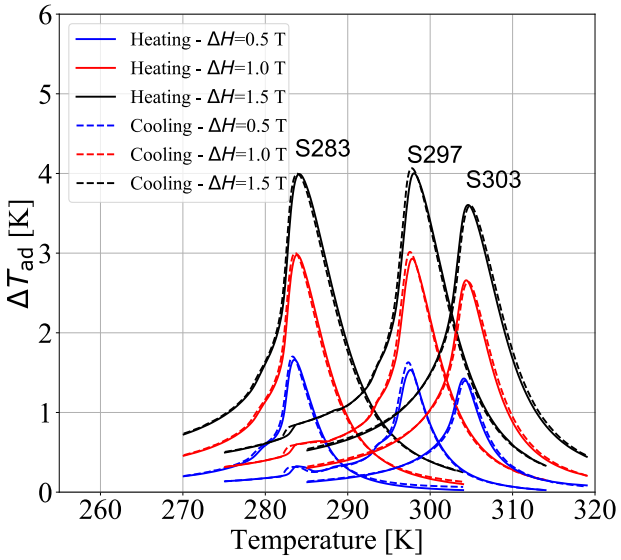

(b)

Figure 5: (color online) (a) Entropy change and (b) adiabatic temperature change as a function of temperature for different applied magnetic field changes.

only simplifies the regenerator assembly, but also facilitates the comparison with the AMR model, which is the main goal of the modelling part of this study. One should bear in mind that the usual precision of the Curie temperatures achieved during the fabrication process is not less than ± 1 K. Rev4C5

The regenerator dimensions and the magnetocaloric material volume fraction were 24.3 ± 0.05 mm (internal diameter), 50 ± 0.05 mm (length) and approximately 55 %, respectively. The regenerator housing was a hollow cylinder made from AISI 304 stainless steel with a wall thickness of 0.5 mm, as shown in Fig. 6. The casing thickness and material were selected based on numerical simulations [41] which demonstrated the existence of a trade-off between the amount of magnetocaloric material, which is directly related to the refrigerating effect, and the combined thermal insulation capability of the casing and intermediate air gap that separates the latter from the magnetic circuit. It was found that thinner casings give rise to higher values of cooling capacity for any regenerator diameter, since the air gap itself provides a better insulation of the AMR than any other material (due to the low thermal conductivity of air). Rev3C4

The regenerator mass was 75 g, with approximately 1/3 of it corresponding to each alloy. The particles were bonded together with epoxy resin, with a mass fraction of 2.7 wt.% (defined as the ratio of the mass of epoxy resin and the mass of magnetocaloric material plus the epoxy resin) to increase the mechanical stability of the AMR, while preserving tortuous pathways for the fluid to flow through. The La-Fe-Si granules were covered with epoxy powder prior to their insertion into the regenerator housing, which was filled with the different layers and slightly compacted to avoid major particle displacement. No separating grids were used. Once the layers were

filled and compacted, the particles were kept fixed using tube caps during the one-step curing process. Rev1C1, Rev4C6 The determination of the regenerator porosity (the fluid volume fraction) will be discussed below together with issues related to the distribution of the epoxy resin inside the porous matrix.

3.2. Experimental Facility and Procedure

The thermal-hydraulic performance of the regenerator was characterized in the experimental facility presented in Fig. 7. A stepper motor (M) drives the magnetic circuit composed of two nested (concentric) Halbach cylinders (NHC). A rectified sinusoidal magnetic field waveform, measured by a Hall effect sensor (H), is produced as the nested cylinders counter rotate around their common axis. The peak value of the magnetic field waveform is 1.69 T [42].

A gear pump and flow limiting valves form the hydraulic power unit (HPU). The flow limiting valves establish the supply pressure and the reservoir pressure. The synchronization between the fluid flow and magnetic field waveforms is achieved with two pairs of solenoid valves, each comprising a low-pressure valve (LPV) and a high-pressure valve (HPV). One valve pair is responsible for the cold blow (CB) and the other for the hot blow (HB). The solenoid valves are controlled using the output signal from the Hall effect sensor, which is also used to compute the cycle frequency.

The displaced fluid mass per blow were determined from the signals of two Coriolis effect mass flow meters (expanded uncertainty of 1%). Minor changes in the blow periods were needed to correct small mass imbalances between the blows. Needle valves were used to adjust the hydraulic resistance in each line.

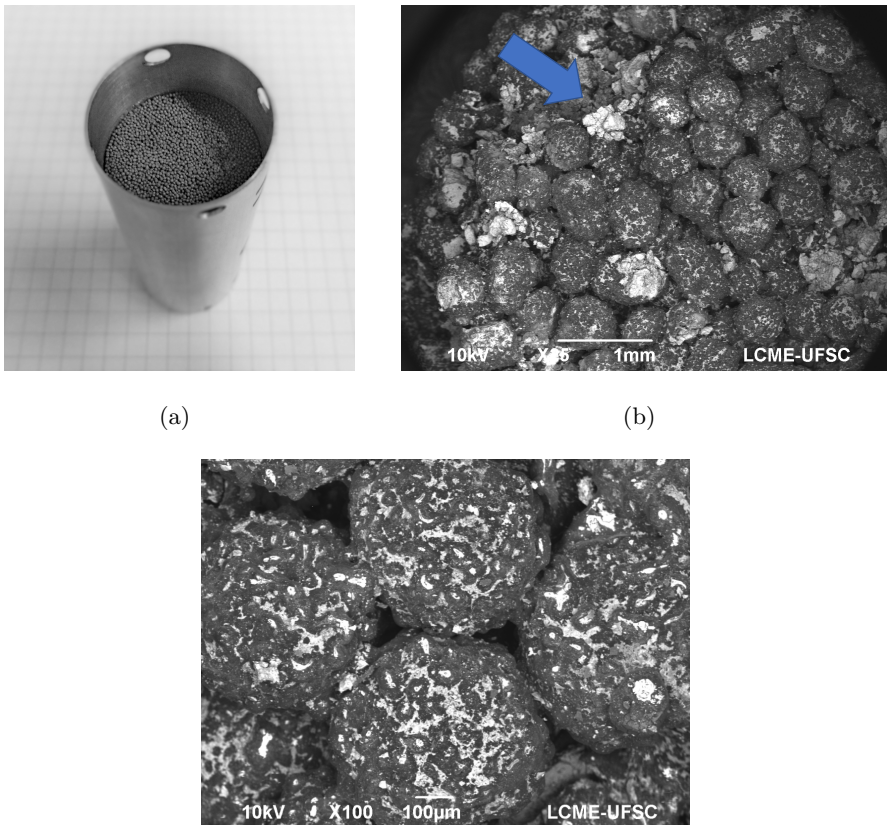

(a) (b)

(c)

Figure 6: (Color online) (a) Photograph of the regenerator bed inside the stainless steel casing, (b) BSE image of the regenerator bed (SEM). The arrow indicates the presence of some loose epoxy, which may be responsible for clogging of the flow passages. (c) BSE zoomed-in image: the white regions are due to electron concentrations in the non-conductive part of the sample (i.e. epoxy). The epoxy resin covers a large portion of the particles and makes some bridges between particles.

Pressure transducers (uncertainty of 0.5 kPa) are used to calculate the pressure drop along the regenerator bed and between the suction and discharge lines of the pump. The AMR inlet temperatures were set by two

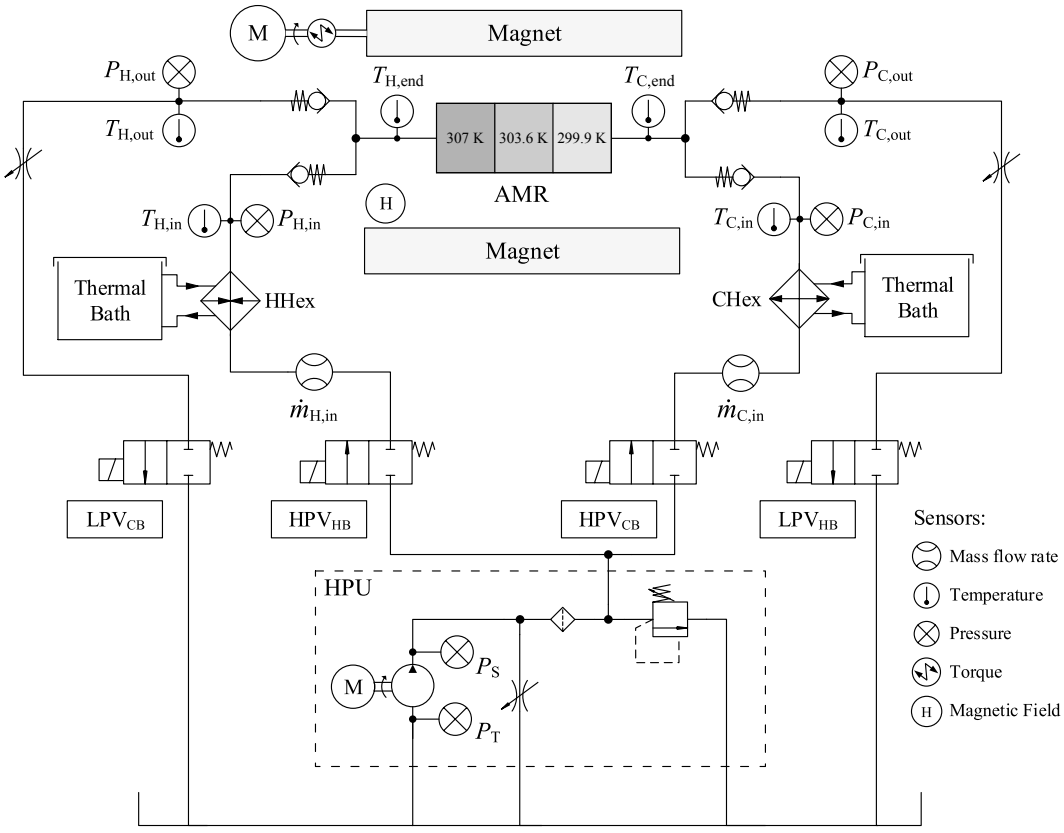

Figure 7: Schematic diagram of the experimental apparatus used to characterize the thermal-hydraulic behavior of the AMR.

temperature-controlled thermal baths. Each side (hot and cold) is equipped with a compact brazed plate heat exchanger (HHex and CHex) to transfer heat between the thermal fluid and the thermal baths. Calibrated T-type thermocouples (uncertainty of 0.15 K) are positioned at several points in the apparatus. Their signals, are used to calculate the cooling capacity and the rejected heat transfer rate.

The operating frequency was kept fixed at 0.5 Hz, while the blow fraction was set at 50 %. This means that 50 % of the total period the material experienced a cold blow, while the other 50 % a hot blow was being executed. During the tests, the ambient temperature was kept at 300 ± 1 K. The heat transfer fluid used in all experiments was a 2 vol.% solution of ENTEK FNE in deionized water. Rev2C5

In one set of tests, the mass flow rate was an independent variable and temperatures of the hot sink and cold source were enforced by changing the temperatures of the hot and cold thermostatic baths emulating the cold thermal source and hot thermal sink on each end of the AMR [42]. To select the hot thermal sink temperature used to evaluate the impact of ΔT_{span} on the cooling power, the AMR was characterized with a fixed temperature span of 5 K and a mass flow rate of 60 kg h^{-1} for different values of the temperature of the hot thermal bath. The hot sink temperature which gave the largest cooling power at that condition was 309.15 K. Therefore, all the other measurements were carried out at this temperature. Table 3 illustrates the operating conditions of the AMR experiments.

Table 3: General parameters of the AMR tests.

Parameter	Value
Frequency	0.5 Hz
Mass flow rate	30 to 60 kg h^{-1}
Blow fraction	50%
T_{hot}	309.15 K
ΔT_{span}	0 to 12 K
H_{max}	1.69 T
Field profile	Rectified cosine
Fluid	2 % wt. ENTEK-water solution
Mass of regenerator	75 g
Regenerator shape	cylinder
Regenerator length	50 mm
Regenerator diameter	24.3 mm
T_C	299.9, 303.5 and 307.0 K
Epoxy amount	2.7 wt.%
Housing material	304 Stainless steel
Housing thickness	0.5 mm

4. Mathematical Modelling

4.1. AMR Geometry

The AMR is treated as a porous medium (packed bed of spheres) with a given regenerator porosity, ε_f, which represents the volume occupied by the fluid phase. As will be seen in this section, a volume-average approach is used, which allows for the conservation equations to be solved without the need to model the transfer processes at the pore scale level.

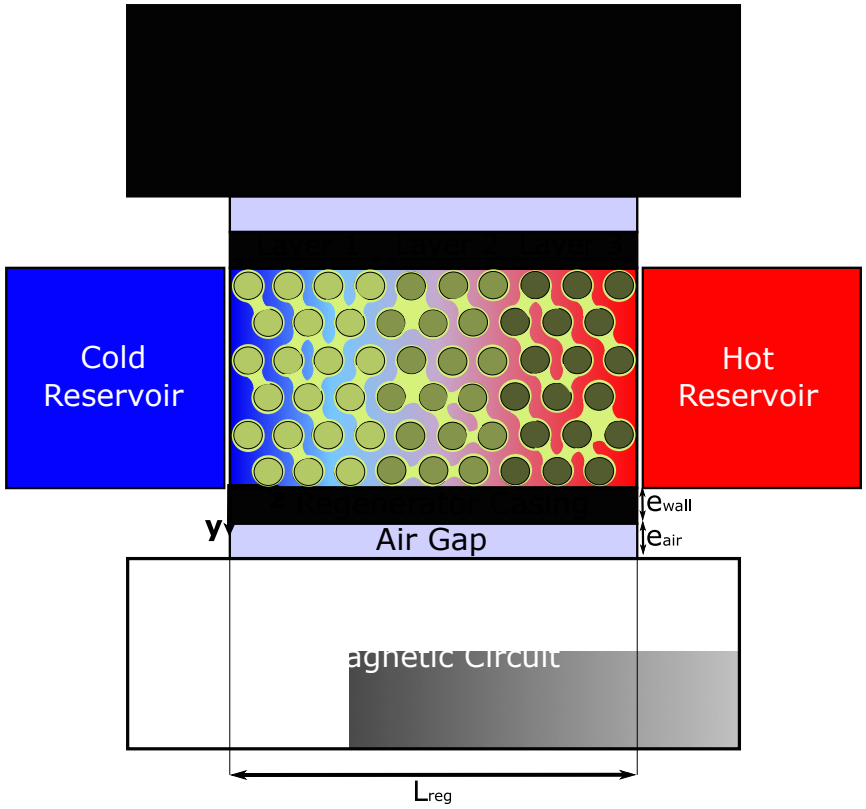

Figure 8: (color online) Schematic model of the regenerator assembly, including the casing, air gap, thermal reservoirs and magnetic circuit. Note that the epoxy resin is shown as a thin layer surrounding each particle and as bridges connecting neighboring particles to illustrate potential blockage of flow passages.

A schematic representation of the model geometry is shown in Fig. 8, which considers not only the regenerator matrix but also its casing and the air gap between the surface of the latter and the magnetic circuit. Calculating the temperature distribution in those media is necessary to determine the heat transfer rate per unit volume through the casing wall.

Figure 8 illustrates the two phases that composed the solid domain,

namely the magnetocaloric material (La-Fe-Si alloy) and the epoxy resin used to bond the MCM particles together and prevent structural damage. As will be seen, the regenerator porosity defined as the volume occupied by the fluid phase, ε_f, is not sufficient to accurately describe the AMR behavior. Thus, a *no-epoxy* porosity, ε, is defined, which represents the volume the fluid phase would occupy if the porous medium was composed only by the magnetocaloric material. The main purpose of the latter is to quantify the energy equation source term related to the magnetocaloric power density and resolve the solid energy equation (to be discussed further ahead). The two porosities are related by: Rev1C2.2

$$\varepsilon_\mathrm{f} = \varepsilon - \frac{m_\mathrm{pm}}{V_\mathrm{pm}} \frac{\varphi_\mathrm{ep}}{\rho_\mathrm{ep}} \tag{2}$$

where,

$$\varepsilon = 1 - \frac{m_\mathrm{pm}}{V_\mathrm{pm}} \frac{(1-\varphi_\mathrm{ep})}{\rho_\mathrm{MCM}} \tag{3}$$

Thus, by definition, ε will always be greater than or equal to ε_f.

The regenerator porosity was determined via independent steady flow isothermal experiments in which the regenerator pressure drop was measured as a function of the fluid flow rate and fitted to the steady-state version of the Brinkman-Forchhheimer equation (see Section 4.2) with ε_f as the only dependent variable. The best results from this fitting ($R^2 = 0.994$) were obtained with a regenerator porosity (fluid volume fraction) of ∼29%.

Given the amount of epoxy added to the regenerator (2.7 wt.%) and the density of the epoxy (∼1150 kg m^{-3}), the fluid volume fraction considering a homogeneous distribution of the epoxy resin in the regenerative matrix should correspond to $\varepsilon_\mathrm{f} \sim 46.5\%$. The discrepancy between the two porosity

values can be attributed to a non-uniform distribution of the epoxy coating on the particles, resulting in blockage of some pores, which reduces the effective cross-section area available for the fluid to flow through the AMR (see Fig. 8). To account for this effect, a third porosity, $\varepsilon_{\text{eff}} = 0.29$, is introduced. Rev1C2.3 Thus, ε_{eff} is used in all fluid related equations to better describe the influence of the epoxy on the thermal-hydraulic behavior of the AMR. In addition to increasing the pressure drop, the epoxy is known to affect the heat transfer in the regenerator in two ways: (i) by reducing the surface area density through pore blockage and (ii) by creating an extra thermal resistance between the fluid and solid phases.

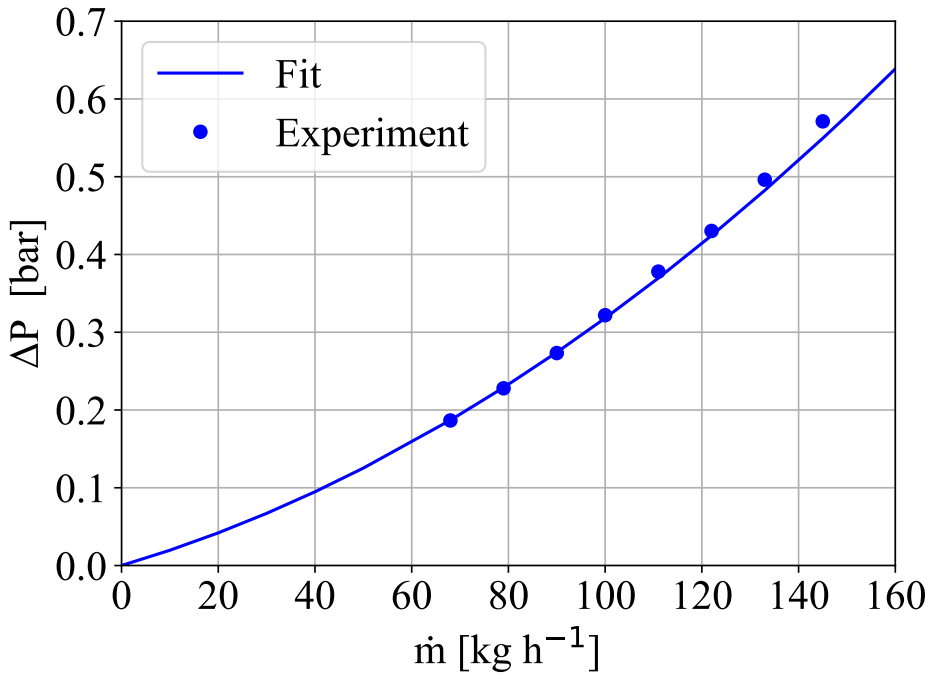

Figure 9: (color online) Fitting of the pressure drop as a function of the mass flow rate in steady flow isothermal experiments. The best fit was obtained for a regenerator porosity $\varepsilon_{\text{eff}} = 29\%$.

The surface area density for a packed bed of spheres with a porosity ε_f is given by: Rev1C2.4, Rev4C9.2

$$\beta = (1 - \varepsilon_\mathrm{f})\frac{6}{d_\mathrm{P}} \tag{4}$$

To account for the reduction in β mentioned above, it is assumed that the surface area density is homogeneously distributed along the regenerator and, therefore, the ratio of the effective and total interfacial surface areas will be the same as the one between the effective and real porosities (ε_eff and ε_f). Thus:

$$\beta_\mathrm{eff} = \frac{\varepsilon_\mathrm{eff}}{\varepsilon_\mathrm{f}}(1 - \varepsilon_\mathrm{f})\frac{6}{d_\mathrm{P}} \tag{5}$$

It is assumed, for calculation and modelling purposes, that all magnetocaloric properties of each material are homogeneous within each layer. Rev3C6

4.2. Momentum Balance

By assuming (i) one-directional flow, (ii) low porosity medium ($\varepsilon_\mathrm{f} < 0.6$), (iii) absence of body forces, and (iv) incompressible flow, the macroscopic momentum equation, also known as the Brinkman-Forchheimer equation, becomes [43] Rev3C5:

$$\frac{\rho_\mathrm{f}}{\varepsilon_\mathrm{eff}}\left(\frac{\partial u}{\partial t}\right) = -\frac{\partial P}{\partial z} - \frac{\mu_\mathrm{f}}{K}u - \frac{c_\mathrm{E}\rho_\mathrm{f}}{K^{1/2}}|u|u \tag{6}$$

The terms in Eq. (6) represent the flow acceleration, pore pressure gradient, microscopic shear stress and microscopic inertial force, respectively. The Ergun constant and permeability were obtained from the Ergun correlations for packed beds of spheres [43, 44]. Since the velocity profile (flow

waveform) in one cycle is an input parameter in the model, this equation can be solved directly for the pressure gradient.

The fluid velocity profile is modelled as a trapezoidal waveform with a 50-% blow fraction [45] for it provides a better fit to the flow rate produced by the gear pump and solenoid valves in the present apparatus. Figure 10 shows the general shape and the parameters of the trapezoidal wave form, where the cycle period is the reciprocal of the operating frequency, $\tau = f^{-1}$.

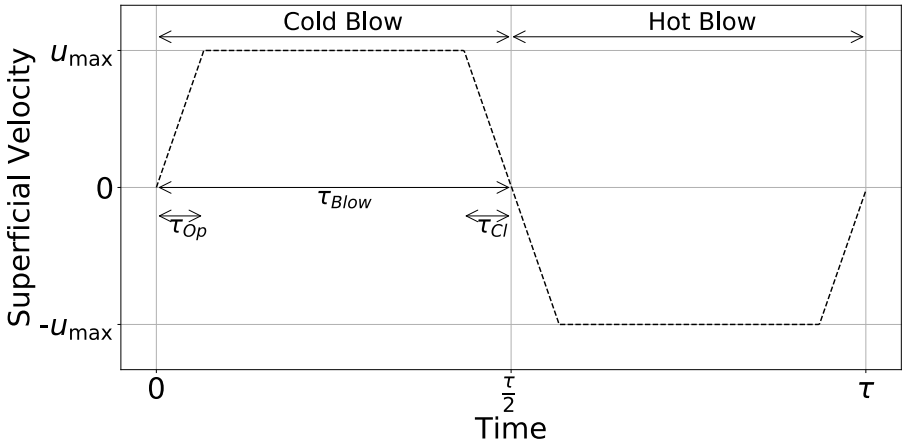

Figure 10: Trapezoidal waveform used to model the fluid flow profile. In addition to the flow period, τ, and the velocity plateau, $u_{\max}$, the parameters needed to describe the waveform are the blow period, τ_{Blow}, the (valve) opening period, τ_{Op}, and the (valve) closing period, τ_{Cl}. For a blow fraction of 50%, $\tau_{Blow} = \tau/2$ and there is a null no-flow period between the hot and cold blows.

The trapezoidal flow velocity profile is described by the following expres-

sion:

$$u(t) = \begin{cases} u_{\max}\frac{t}{\tau_{\text{Ramp}}}, & \text{if} \quad 0 \leq t < \tau_{\text{Ramp}} \\ u_{\max}, & \text{if} \quad \tau_{\text{Ramp}} \leq t < \tau_{\text{Blow}} - \tau_{\text{Ramp}} \\ u_{\max}\frac{\tau_{\text{Blow}}}{\tau_{\text{Ramp}}} - u_{\max}\frac{t}{\tau_{\text{Ramp}}}, & \text{if} \quad \tau_{\text{Blow}} - \tau_{\text{Ramp}} \leq t < \tau_{\text{Blow}} \\ -u(t - \frac{\tau}{2}), & \text{if} \quad \tau_{\text{Blow}} \leq t < \tau \end{cases} \tag{7}$$

where, based on comparisons with the experimental instantaneous AMR pressure gradient, the (valve) opening and closing periods, τ_{Op} and τ_{Cl}, are assumed identical and equal to a ramp time, $\tau_{\text{Ramp}} \approx \tau/15$. $u_{\max}$ is calculated from the average mass of fluid displaced per blow.

4.3. Fluid-Phase Energy Balance

The macroscopic energy balance for the fluid phase is given by:

$$\rho_{\text{f}} c_{\text{p,f}} \left(\varepsilon_{\text{eff}} \frac{\partial T_{\text{f}}}{\partial t} + u \frac{\partial T_{\text{f}}}{\partial z} \right) = h_{\text{eff}} \beta_{\text{eff}} (T_{\text{s}} - T_{\text{f}}) + u \left| \frac{\partial P}{\partial z} \right| + \varepsilon_{\text{eff}} [k_{\text{f}}^{\text{eff}} + \rho_{\text{f}} c_{\text{p,f}} D_{||}] \frac{\partial^2 T_{\text{f}}}{\partial z^2} + \dot{q}_{\text{csg}} \tag{8}$$

where β_{eff} is the corrected interstitial surface area density of the pores, $k_{\text{f}}^{\text{eff}}$ is the effective thermal conductivity of the fluid phase ($k_{\text{f}}^{\text{eff}} = \varepsilon_{\text{eff}} k_{\text{f}}$) [46], and $D_{||}$ is the longitudinal thermal dispersion constant, calculated using the correlation proposed in Ref. [47]:

$$\frac{D_{||}}{\alpha_{\text{f}}} = \left(\frac{Pe_{\text{dp}}}{2} \right)^2 \frac{\sqrt{2}}{60(\sqrt{1 - \varepsilon_{\text{eff}}})} \quad \text{for} \quad \left(\frac{Pe_{\text{dp}}}{2} \right)^2 < 1 \tag{9}$$

Rev4C9.1

$$\frac{D_{||}}{\alpha_{\text{f}}} = 0.75 \frac{Pe_{\text{dp}}}{2} \quad \text{for} \quad \frac{Pe_{\text{dp}}}{2} > 1 \tag{10}$$

The terms on the left side of Eq. (8) are related to the thermal capacity and longitudinal advection, and the ones on the right are due to interstitial heat transfer, viscous dissipation, axial conduction in the porous medium [46] and heat transfer between the porous medium and the regenerator casing, respectively. The latter term will be discussed in Section 4.5. Since the equation is solved along a cycle, the temperature at the end of the cycle must be equal to the temperature at the beginning ($T_\mathrm{f}|_{t=\tau} = T_\mathrm{f}|_{t=0}$), which is the temporal boundary condition. The spatial boundary conditions will not be the same for every instant as they depend on the type of blow (cold blow or hot blow):

$$\begin{aligned} &\text{Cold blow } (u>0) \begin{cases} T_\mathrm{f}|_{z=0} = T_\mathrm{cold} \\ \frac{\partial T_\mathrm{f}}{\partial z}\big|_{z=L} = 0 \end{cases} \\ &\text{Hot blow } (u<0) \begin{cases} T_\mathrm{f}|_{z=L} = T_\mathrm{hot} \\ \frac{\partial T_\mathrm{f}}{\partial z}\big|_{z=0} = 0 \end{cases} \end{aligned} \tag{11}$$

The effective interstitial heat transfer coefficient, h_eff, is calculated from the following expression [48]:

$$h_\mathrm{eff} = H_\mathrm{D} h = \frac{h}{1 + \frac{Bi}{5}\chi\,(Fo)} \tag{12}$$

where h is the uncompensated interstitial heat transfer coefficient between the fluid and solid phases, calculated through the Nusselt number correlation for packed beds of spheres proposed in Ref. [49]:

$$Nu_\mathrm{dp} = \frac{h d_\mathrm{p}}{k_\mathrm{f}} = 2\left[1 + \frac{4(1-\varepsilon_\mathrm{eff})}{\varepsilon_\mathrm{eff}}\right] + (1-\varepsilon_\mathrm{eff})^{1/2} Re_\mathrm{dp}^{0.6} Pr^{1/3} \tag{13}$$

where $Re_{\mathrm{dp}} = \frac{\rho_{\mathrm{f}} u d_{\mathrm{P}}}{\mu_{\mathrm{f}}}$.

In Eq. (12), H_{D} is the modified Hausen degradation factor [48] which quantifies the reduction of the interstitial heat transfer associated with spatial and temporal temperature variations within the solid matrix caused by the finite solid thermal conductivity and cyclical changes of the fluid temperature flowing through the matrix. These two effects are epitomized by the Biot and Fourier numbers which, for the epoxy coated spherical particles, are defined as follows:

$$Bi = \frac{h L_{\mathrm{c}}}{k_{\mathrm{eq}}} \tag{14}$$

and:

$$Fo = \frac{k_{eq} \tau}{(\rho c)_{eq} L_{\mathrm{c}}^2} \tag{15}$$

where L_{c} is the characteristic length of an epoxy coated sphere given by:

$$L_c = \frac{d_{\mathrm{P}}}{6} + L_{\mathrm{ep}} \tag{16}$$

where the first term is the characteristic length of the magnetocaloric sphere (volume to exposed surface area ratio) and the second term is the thickness of the epoxy coating calculated as:

$$L_{\mathrm{ep}} = \frac{1}{2}\left[d_{\mathrm{P}} \left(\frac{\varepsilon - \varepsilon_{\mathrm{f}}}{1 - \varepsilon} + 1 \right)^{\frac{1}{3}} - 1 \right] \tag{17}$$

To arrive at Eq. (17), the following assumptions are made: (i) the bed is composed of perfectly spherical, mono-disperse particles, (ii) the epoxy completely covers the spheres and is homogeneously distributed along the regenerator, so that all spheres are covered with the same epoxy thickness. Rev1C2.1

The equivalent thermal conductivity of the composite solid (magnetocaloric material and epoxy coating) is given by the following relationship derived from the combined thermal resistance of the two concentric media (see Fig. 11):

$$k_{\mathrm{s}}^{\mathrm{eq}} = \left(\frac{d_{\mathrm{P}}}{6} + L_{\mathrm{ep}}\right)\left(\frac{d_{\mathrm{P}}}{6k_{\mathrm{s}}} + \frac{L_{\mathrm{ep}}}{k_{\mathrm{ep}}}\right)^{-1} \tag{18}$$

where $k_{\mathrm{s}} = 8$ W m^{-1} K $^{-1}$ and $k_{\mathrm{ep}} = 0.25$ W m^{-1} K $^{-1}$. Note that to obtain Eq. (18), it is assumed that the epoxy layer is so thin that the heat conduction through the epoxy layer can be calculated as if through a plane wall. Rev1C2.1 - aparece 2 vezes

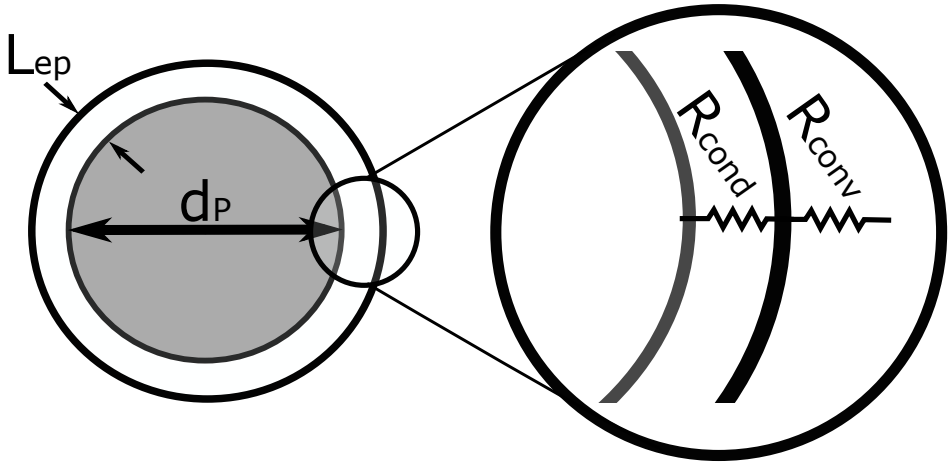

Figure 11: Representation of a sphere of MCM covered by epoxy with the respective thermal resistances due to conduction in the epoxy layer, R_{cond} and convection in the fluid, R_{conv}.

The volumetric heat capacity of the composite solid, $(\rho c)_{\mathrm{eq}}$, is calculated from a mass weighted average of the volumetric heat capacities of the two layers.

In Eq. 12, $\chi(Fo)$ is an empirical parameter that embodies the dependence of the degradation factor on the Fourier number given by [48]:

$$\chi(Fo) = Fo \exp\left\{0.246196 - 0.84878 \ln(Fo) - 0.05639 [\ln(Fo)]^2\right\} \quad (19)$$

4.4. Solid-Phase Energy Balance

For the solid phase, the macroscopic energy balance is given by:

$$\rho_s c_s (1-\varepsilon)\frac{\partial T_s}{\partial t} = h_{eff}\beta_{eff}(T_f - T_s) + (1-\varepsilon)k_s^{eff}\frac{\partial^2 T_s}{\partial z^2} + \dot{q}_{MCE} \quad (20)$$

where the term on the left represents the thermal capacity of the solid, while the terms on the right represent the interstitial heat transfer, axial conduction in the porous medium and the magnetocaloric effect (source term). The effective thermal conductivity of the solid, k_s^{eff}, was determined with the correlation proposed in Ref. [50]: Rev4C9.3

$$\frac{k_s^{eff}}{k_f} = (1-\alpha_0)\frac{\varepsilon_f f_0 + (1-\varepsilon_f f_0)\frac{k_s^{eq}}{k_f}}{1-\varepsilon_f(1-f_0)+\frac{k_s^{eq}}{k_f}\varepsilon_f(1-f_0)} + \alpha_0\frac{2(\frac{k_s^{eq}}{k_f})^2(1-\varepsilon_f)+(1+2\varepsilon_f)\frac{k_s^{eq}}{k_f}}{(2+\varepsilon_f)\frac{k_s^{eq}}{k_f}+(1-\varepsilon_f)} \quad (21)$$

where $f_0 = 0.8$ and $\log\alpha_0 = -1.084 - 6.778(\varepsilon_f - 0.298)$ for $0.298 < \varepsilon_f < 0.58$.

In the present study, $\dot{q}_{MCE}$ is implemented via the built-in method, which is usually employed when the applied magnetic field changes continuously over time [43]. The source term is given by [22, 48]:

$$\dot{q}_{MCE}(t,z) = -\rho_s(1-\varepsilon)T_s\frac{\partial s(H,T_s)}{\partial H}\frac{\partial H}{\partial t} \quad (22)$$

Note that Eq. (22) is based on the volume fraction of the magnetocaloric material, ε, since the epoxy does not exhibit MCE. The value of $\frac{\partial s}{\partial H}$ is calculated from the adiabatic temperature change and specific heat capacity data for the $La(Fe,Mn,Si)_{13}H_y$ alloys using the following thermodynamic relationship:

$$\frac{c_s}{T_s}\, dT_{ad} = -\frac{\partial s}{\partial H} dH \tag{23}$$

whereby the temperature change provoked by the change in magnetic field is calculated as an equivalent change in entropy, which satisfies the overall energy balance.

The boundary conditions for the solid phase are independent of the type of blow and, together with the periodic temporal condition, are given by:

$$\begin{aligned} T_s|_{t=\tau} &= T_s|_{t=0} \\ \left.\frac{\partial T_s}{\partial z}\right|_{z=0} &= 0 \\ \left.\frac{\partial T_s}{\partial z}\right|_{z=L} &= 0 \end{aligned} \tag{24}$$

4.5. Casing Heat Transfer

The thermal transfer through the regenerator casing, $\dot{q}_{csg}$ (see Eq. 8), was calculated as:

$$\dot{q}_{csg} = h_{wall} \frac{p_{c,reg}}{A_{c,reg}} (T_f - T_{wall}|_{y=0}) \tag{25}$$

where h_{wall} is the heat transfer coefficient between the flowing fluid through the porous matrix and the inner wall of the regenerator casing given by the

relation proposed in Ref. [51]:

$$Nu_{\mathrm{dp}}^{\mathrm{wall}} = \frac{h_{\mathrm{wall}} d_{\mathrm{P}}}{k_{\mathrm{f}}} = 0.17 Re_{\mathrm{dp}}^{0.79} \text{ for } 20 \leq Re_{\mathrm{dp}} \leq 7600 \tag{26}$$

$T_{\mathrm{wall}}|_{y=0}$ is calculated by solving the heat conduction equation in the casing wall. Assuming uniform properties and a negligible radius of curvature for the regenerator wall, one has:

$$\frac{\partial T_{\mathrm{wall}}}{\partial t} = \alpha_{\mathrm{wall}} \left(\frac{\partial^2 T_{\mathrm{wall}}}{\partial y^2} + \frac{\partial^2 T_{\mathrm{wall}}}{\partial z^2} \right) \tag{27}$$

which, similarly to the solid phase of the porous media, is assumed to be insulated at both ends ($\frac{\partial T_{\mathrm{wall}}}{\partial z}\big|_{z=0} = \frac{\partial T_{\mathrm{wall}}}{\partial z}\big|_{z=L} = 0$). The wall at $y = 0$, which is in contact with the porous media, has a convective boundary condition given by:

$$q''_{\mathrm{wall}} = h_{\mathrm{wall}} (T_{\mathrm{f}} - T_{\mathrm{wall}}|_{y=0}) \tag{28}$$

For the wall at $y = e_{\mathrm{wall}}$, which is in contact with the air gap, the boundary condition is given by the continuity of heat fluxes as follows:

$$k_{\mathrm{air}} \frac{\partial T_{\mathrm{air}}}{\partial y}\bigg|_{y=e_{\mathrm{wall}}} = k_{\mathrm{wall}} \frac{\partial T_{\mathrm{wall}}}{\partial y}\bigg|_{y=e_{\mathrm{wall}}} \tag{29}$$

Eq. (29) is solved together with the energy balance in the air gap, given by (assuming uniform properties):

$$\frac{\partial T_{\mathrm{air}}}{\partial t} = \alpha_{\mathrm{air}} \left(\frac{\partial^2 T_{\mathrm{air}}}{\partial y^2} + \frac{\partial^2 T_{\mathrm{air}}}{\partial z^2} \right) + \alpha_{\mathrm{air}} \frac{\dot{q}_{\mathrm{air}}}{k_{\mathrm{air}}} \tag{30}$$

where $\dot{q}_{\mathrm{air}}$ is the viscous dissipation rate per unit volume given by:

$$\dot{q}_{\mathrm{air}} = \mu_{\mathrm{air}} \left(\frac{\omega R}{e_{\mathrm{air}}} \right)^2 \tag{31}$$

The air gap is also assumed to be insulated at both ends ($\frac{\partial T_{\text{air}}}{\partial z}\big|_{z=0} = \frac{\partial T_{\text{air}}}{\partial z}\big|_{z=L} = 0$) and its bottom boundary condition is given by Eq. (29). Due to its large mass, the magnetic circuit is assumed isothermal and in thermal equilibrium with the ambient. Therefore, the upper boundary condition of the air gap is a prescribed temperature ($T_{\text{air}} = T_{\text{amb}}$).

4.6. Solution Method

The governing equations were solved via the finite volume method, according to the procedure outlined in Ref. [43]. However, some improvements were made particularly in the property calculation (e.g., Eq. 23) and mesh generation routines, enabling the solution of regenerators with any given number of material layers. More specifically, Eq. (23) was used to determine the value of $\frac{\partial s}{\partial H}$. Since the derivative is treated as any other MCM property, it was calculated at a given temperature and effective field (see Section 4.6) by interpolating between the values of neighboring points. The interpolation steps for the temperature and effective field density were 0.1 K and 0.01 T, respectively. Rev4C11.1 Additionally, in the present approach, no single elemental volume in the regenerator can have materials with two or more distinct Curie temperatures (i.e., two or more different MCMs). As a result, the mesh distribution is not necessarily homogeneous. Finally, to accelerate the numerical convergence, more volumes were concentrated in the layers closest to the ends of the regenerator. Rev4C11.2

As suggested in Ref. [52], in the momentum equation, the fluid properties are evaluated at a mean fluid temperature, allowing for the momentum and energy equations to be solved independently. Physical properties of pure water were considered. The modelling independent parameters (frequency, mass flow rate etc.) are identical to the ones used in the experiments de-

scribed in Section 3.1. As for the magnetocaloric properties of the solid matrix, a special procedure needs to be used due to the different Curie temperatures of each layer, as outlined below.

4.7. Physical Properties Implementation

The property estimation procedure involves using the experimentally determined properties (see Section 2.2) for one specific alloy composition (one specific T_C) as a reference for all layers of the regenerator. This means that all layers are assumed to have the same properties as the reference, but shifted along the temperature axis to match their respective T_C's. An example of this procedure is shown in Figure 12 where the values of c_s/T of the reference composition ($T_\mathrm{C} = 298.6$ K) is shifted to represent the properties of another alloy with a Curie temperature of 288.6 K. Note that apart from the position along the temperature axis, both property profiles are exactly the same. As already seen in Section 2.2, this assumption is not exact, since the c_s curves for the three materials exhibit some small differences with respect to each other. However, the consequences of such differences to the AMR model are expected to be small.

The property shift described above has been used to determine other properties, namely the specific entropy and its derivative with respect to the applied field $\left(\frac{\partial s}{\partial H}\right)$. The reason for applying the shift to c_s/T instead of the specific heat itself can be explained using its definition:

$$c_\mathrm{s} = T_\mathrm{s} \left.\frac{\partial s}{\partial T}\right|_H \tag{32}$$

Note that the temperature is used to determine the specific heat, therefore, displacing it along the temperature axis would effectively change the equiv-

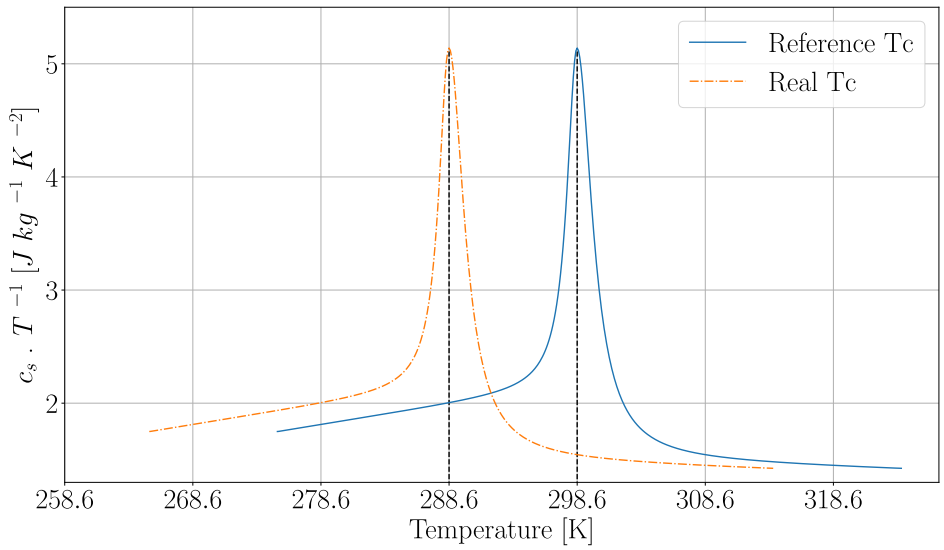

Figure 12: (color online) Example of the c_s/T shifting procedure used to calculate magnetocaloric properties for any given T_C.

alent value of the entropy derivative, rendering the specific heat and entropy inconsistent. On the other hand, applying the shift to c_s/T is equivalent to shifting $\frac{\partial s}{\partial T}|_H$ directly, thus avoiding any possible inconsistency. The specific heat can then be calculated simply by multiplying the latter value by the temperature.

4.8. Applied Field Profile and Demagnetizing Effects

Demagnetization effects were quantified via a simplified approach that considers each elemental control volume to be (locally) isothermal [53]. Therefore, the effective magnetic field can be calculated from the following scalar relationship:

$$H_{\text{eff}} = H_{\text{apl}} - N_{\text{D}} M(H_{\text{apl}}, T) \tag{33}$$

where H_{apl} is the applied magnetic field generated by the magnetic circuit, M is the magnetization and N_{D} is the demagnetization factor computed from contributions due to the casing geometry, $N_{\mathrm{D,csg}}$, and matrix geometry, $N_{\mathrm{D,geo}}$. For a packed bed of spheres [54]:

$$N_{\mathrm{D}} = N_{\mathrm{D,geo}} + (1-\varepsilon)(N_{\mathrm{D,csg}} - N_{\mathrm{D,geo}}) \tag{34}$$

where $N_{\mathrm{D,geo}} = 1/3$ [54]. Note that in Eq. (34) the no-epoxy porosity was used. The casing demagnetization factor for a cylindrical regenerator is estimated from [55]:

$$N_{\mathrm{D,csg}} = \frac{\frac{L_{\mathrm{reg}}}{D_{\mathrm{reg}}}}{2\frac{L_{\mathrm{reg}}}{D_{\mathrm{reg}}} + 1} \tag{35}$$

Figure 13 compares the effective magnetic flux density and the applied magnetic flux density, as predicted and experimentally validated in Ref. [56]. As can be seen, a reduction of the order of 20% is observed at the peak.

5. AMR Performance Results and Discussion

The typical AMR pressure drop behavior is shown in Fig. 14, which presents the experimental and numerical results for the pressure drop in the regenerator during one cycle. Although the model is unable to perfectly capture the transients associated with the change of direction and acceleration of the fluid flow in the regenerator (the model assumes a trapezoidal waveform), the steady portions of the instantaneous experimental pressure drop are well predicted. Another important aspect is the symmetric behavior of the experimental curves in the hot and cold blows, which is an indication that the hydraulic resistance of the AMR is equivalent in both directions.

A comparison between the experimental and numerical average pressure drops for all conditions is shown in Fig. 15. In the model, the average

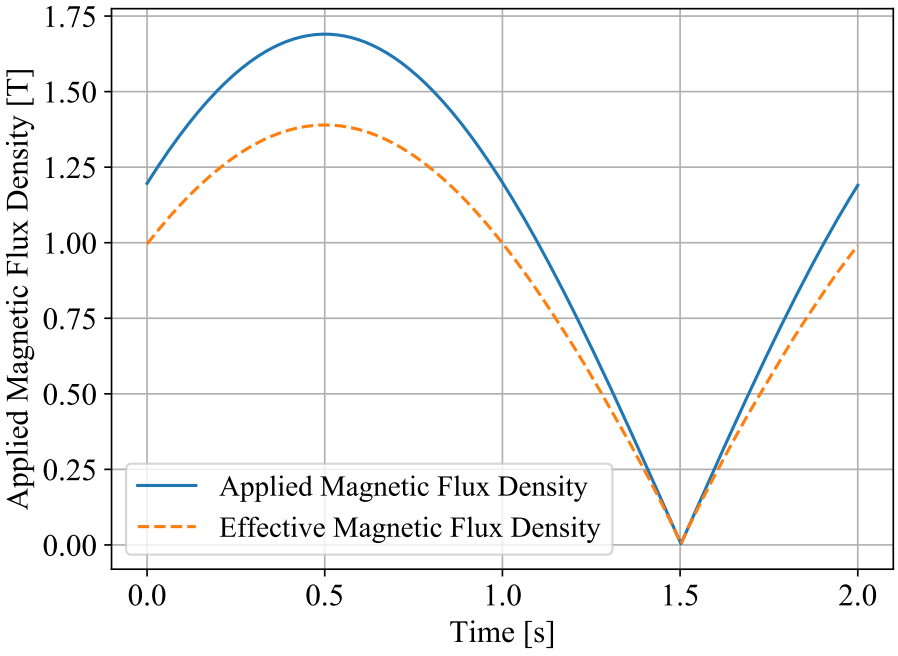

Figure 13: Comparison between the applied and effective magnetic flux density at the center point of the regenerator during a cycle.

pressure drop is simply the amplitude of the square wave. Each cluster of points represents one of the four mass flow rates analysed (30, 40, 50 and 60 kg h^{-1}). There is a generally good agreement between the predictions and the data, with deviations always smaller than 15%, despite the small tendency for the model to overestimate the pressure drop in lower mass flow rates. It was also observed that, in the model, an increase in the temperature span always increases the pressure drop due to changes in fluid properties. In the experiments, however, this trend was not verified, as the results for a temperature span of 9 K showed a consistently higher pressure drop. This behavior could be due to slight deviations from the nominal

values of the operating conditions (e.g., mass flow rate) during the tests for this temperature span, since most of the other results show a direct relation between the temperature span and an increase in pressure drop. Even with those differences, the agreement is acceptable, showing that the fitting of the pressure drop using steady flow data described in Section 4.1 can be extrapolated to the periodic blows taking place in the regenerator.

Clearly, a high pressure drop is the main disadvantage of packed beds of spheres and irregular particles, which is one the highest among the matrices used in magnetic refrigeration. This effect is exacerbated when there is potential pore blockage due to non-uniform epoxy distribution. There are other disadvantages to using packed beds, such as the multiple points of contact between particles, which induce axial conduction in the matrix (a thermal loss). Nonetheless, the main advantage of using particles is cost, which is lower than structured porous medium geometries, such as pins, microchannels and parallel plates. Another advantage is a higher interstitial heat transfer coefficient, which always increases with the mass flow rate for it is directly proportional to Re_{dp} [57]. For microchannels and plates, however, if the flow is laminar, then the heat transfer coefficient is constant and the thermal conductance does not change with the mass flow rate. Rev4C21

The instantaneous temperature behavior at the cold and hot ends of the regenerator is another important variable in the evaluation of the performance of the mathematical model. The profiles shown in Fig. 16 were obtained with a mass flow rate of 40 kg h^{-1} for a ΔT_{span} of 6 K and with a mass flow rate of 60 kg h^{-1} for a ΔT_{span} of 12 K. Nevertheless, the overall good agreement between the data and the numerical results was observed in all cases tested, particularly at the hot side. The sharp changes observed in the numerical temperature profiles (at $t = 1$ s for the hot end temperature,

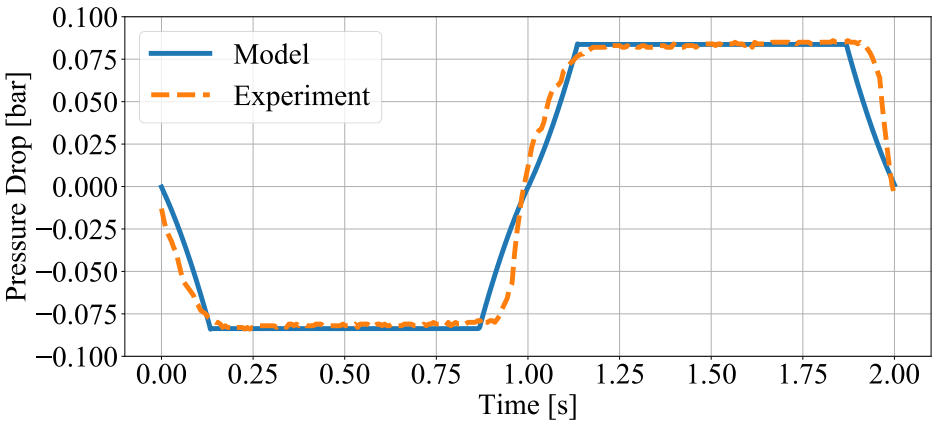

Figure 14: (color online) Numerical and experimental results for the instantaneous pressure drop in the regenerator for a mass flow rate of 40 kg h^{-1} and span of 12 K between the thermal reservoirs.

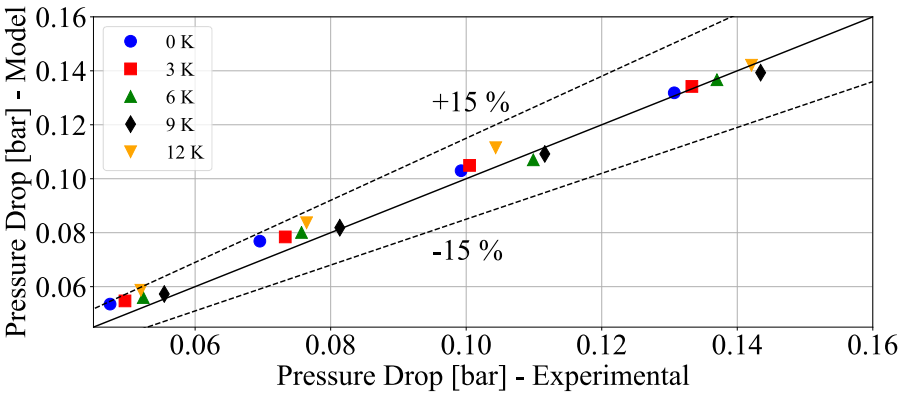

Figure 15: (color online) Comparison between numerical and experimental average pressure drop results in the regenerator for all mass flow rates and temperature spans.

red solid curve, and at $t = 0$ and/or $t = 2$ s for the cold end temperature, blue solid curve) are due to the changes in flow direction (between the hot to cold blow and vice-versa), according to the fluid flow waveform (Fig. 10).

Unlike the numerical profiles, the experimental fluid temperatures at $t = 0$ and $t = \tau$ are not exactly the same because one cycle will always be different from the next, even after the periodic steady state is attained. That said, the differences are still quite small (of the order of 0.36 K for the 40-kg/h 6-K temperature span case of Fig. 16.a), indicating that the periodic steady state is achieved in the experiment as well. This, in itself, is also a clear indication of the mechanical stability of the regenerative matrix. Rev4C20

Finally, the AMR performance curves are presented in Fig. 17, comparing the experimental data and numerical results for the specific cooling capacity as a function of ΔT_{span} for different cycle averaged mass flow rates. The typical response of increasing the zero-span cooling capacity and decreasing the zero-load ΔT_{ad} is observed. The small differences between them can be attributed to dead volume effects and thermal losses in the hydraulic components, such as valves and tubing. Again, the regenerator was able to run for dozens of hours, showing no sign of loss of mechanical integrity (immediately perceived due to a progressive increase of the experimental AMR pressure drop, and confirmed through visual inspection of the matrix after disassembly of the regenerator). This is a significant improvement compared to irregular particles, which have been reported to break during operation [58]. Rev4C22

6. Conclusion

The present paper conducted an extensive analysis of spheroidal particles of $La(Fe,Mn,Si)_{13}H_y$ alloys in terms of their magnetocaloric properties and thermal performance when arranged as a three-layer AMR. The main findings of the study are summarized as follows:

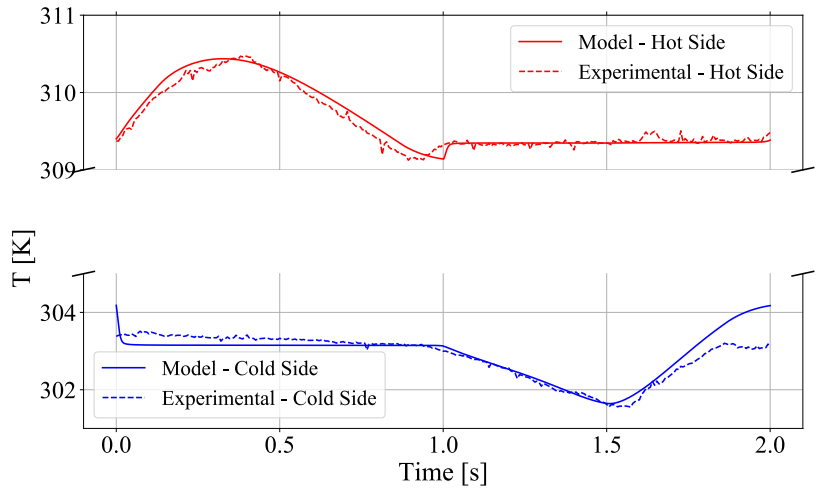

(a)

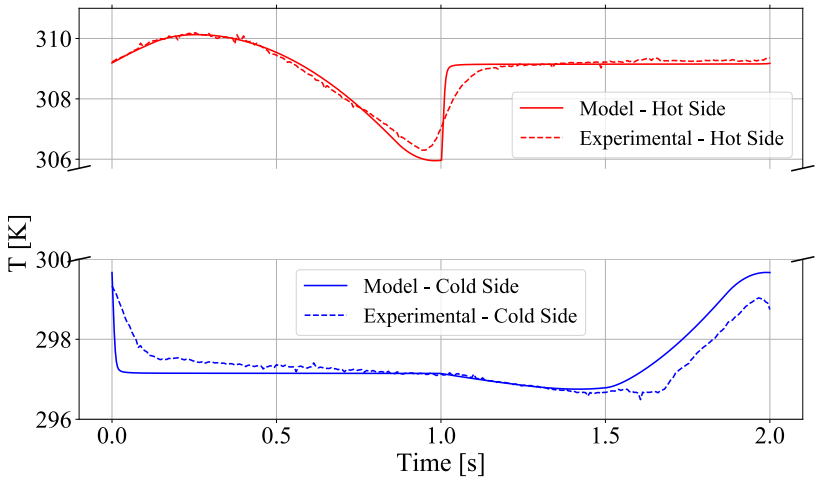

(b)

Figure 16: (Color online) Comparison between the numerical and experimental instantaneous temperature profiles at the hot and cold ends of the regenerator during one cycle. In both cases, the cycle frequency is 0.5 Hz, and the mass flow rates and temperature span between the thermal reservoirs are (a) 40 kg h^{-1} and ΔT_{span} of 6 K and (b) 60 kg h^{-1} and ΔT_{span} of 12 K.

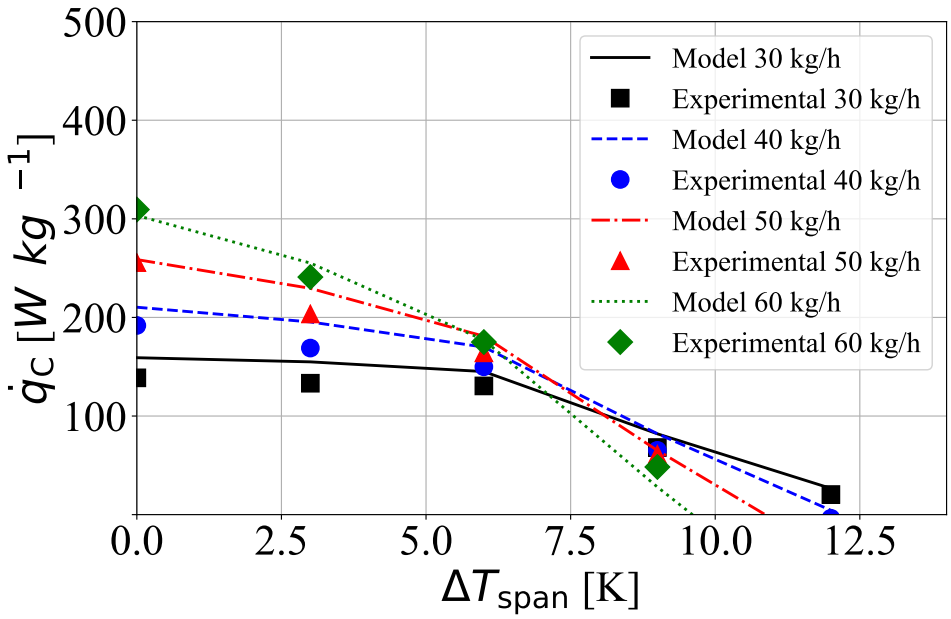

Figure 17: (Color online) AMR performance curves (experimental data vs. model results) for the spheroidal particle AMR for mass flow rates of 30, 40, 50 and 60 kg h^{-1}. The cycle frequency was 0.5 Hz, while the hot heat sink temperature was 309.15 K.

1. The large $\alpha-$Fe content and porosity of the spheroidal granules (compared with the irregular shaped particles investigated in previous studies) confirmed the possibility of enhancing the mechanical properties of the active magnetic regenerator, which has endured dozens of hours of cycling without any perceivable loss of integrity (quantified by stable measurements of pressure drop and fluid temperature at the hot and cold ends of the regenerator);
2. As expected, the large $\alpha-$Fe content was also responsible for a reduction of the magnetocaloric effect which, when combined with non-homogeneities in the spatial distribution of the epoxy binder (which give rise to pore blockage and creates preferential flow paths within

the porous medium), can significantly deteriorate the specific cooling capacity of the AMR. Therefore, further work in the art of regenerator assembly should be focused at improving the structural reliability of the AMR while preserving the open pore matrix. Despite the difficulties involved, further studies on the bonding process are under way to evaluate the variation of some parameters such as the epoxy type, curing time and curing temperature, regenerator position while curing, among others. Elimination of the epoxy bonding agent from the assembly process is also under investigation to enable a more effective use of spheroidal $La(Fe,Mn,Si)_{13}H_y$ particles in prototypes operating in actual (relevant) conditions;

3. The AMR mathematical framework took into account several unique features of the present system, such as the trapezoidal fluid flow waveform produced by the gear pump-solenoid valve assembly and a detailed model for the influence of the epoxy resin on the regenerator thermal-hydraulic performance. Thus, it was capable of predicting the instantaneous pressure drop of the oscillating flow, as well as the instantaneous temperatures at both ends of the AMR with an encouraging agreement. Also, the performance curves for a wide range of conditions were predicted with average deviations smaller than 7% for the zero-span cooling capacity. The shifting procedure adopted to calculate the magnetocaloric properties of the $La(Fe,Mn,Si)_{13}H_y$ alloys was preliminary validated through the comparison between the numerical model and experimental data. Further work associated with the model involves incorporating the dead-volume losses and validating the model with experimental data for regenerators with a larger number of layers.

Acknowledgements

The Authors appreciate the support from CODEMGE and EMBRAPII through Grant No. 201813442 ("Development of an Air Conditioner Operated by a Magnetic Cooling Unit" Project). Additional funding was provided by CAPES (Talents for Innovation Program - Grant No. 88887.194773/2018-00) to H. Neves Bez and J. Lozano, and by the National Institutes of Science and Technology (INCT) Program (CNPq Grant No. 443696/2014-4; FAPESC Grant No. 2018TR1576). Technical support from LCME-UFSC for the electron microscopy work (LCME-MAT 2020) and LABCAM-UFSC is duly acknowledged. The authors are grateful to Alan T.D. Nakashima for helping with the preparation of Figure 7.

References

[1] A. Smith, C. R. H. Bahl, R. Bjørk, K. Engelbrecht, K. K. Nielsen, N. Pryds, Materials challenges for high performance magnetocaloric refrigeration devices, Advanced Energy Materials 2 (2012) 1288–1318.

[2] S. Crossley, N. D. Mathur, X. Moya, New developments in caloric materials for cooling applications, AIP Advances 5 (2015) 067153.

[3] S. Fähler, V. K. Pecharsky, Caloric effects in ferroic materials: New concepts for cooling, MRS Bulletin 43 (2018) 264–268.

[4] S. M. Kirsch, F. Welsch, N. Michaelis, M. Schmidt, A. Wieczorek, J. Frenzel, G. Eggeler, A. Schutze, S. Seelecke, NiTi-based elastocaloric cooling on the macroscale: From basic concepts to realization, Energy Technology 6 (2018) 1567–1587.

[5] A. Kitanovski, U. Plaznik, U. Tomc, A. Poredos, Present and future caloric refrigeration and heat-pump technologies, International Journal of Refrigeration 57 (2015) 288–298.

[6] S. Qian, D. Nasuta, A. Rhoads, Y. Wang, Y. Geng, Y. Hwang, R. Radermacher, I. Takeuchi, Not-in-kind cooling technologies: A quantitative comparison of refrigerants and system performance, International Journal of Refrigeration 62 (2016) 177–192.

[7] J. Liu, T. Gottschall, K. P. Skokov, J. D. Moore, O. Gutfleisch, Giant magnetocaloric effect driven by structural transitions, Nature Materials 11 (2012) 620–626.

[8] A. Waske, M. E. Gruner, T. Gottschall, O. Gutfleisch, Magnetocaloric materials for refrigeration near room temperature, MRS Bulletin 43 (2018) 269–273.

[9] V. Franco, J. Blázquez, B. Ingale, A. Conde, The magnetocaloric effect and magnetic refrigeration near room temperature: Materials and models, Annual Review of Materials Research 42 (2012) 305–342.

[10] J. Lyubina, R. Schäfer, N. Martin, L. Schultz, O. Gutfleisch, Novel design of $La(Fe,Si)_{13}$ alloys towards high magnetic refrigeration performance, Advanced Materials 22 (2010) 3735–3739.

[11] W. Brey, G. Nellis, S. Klein, Thermodynamic modeling of magnetic hysteresis in AMRR cycles, International Journal of Refrigeration 47 (2014) 85–97.

[12] L. von Moos, C. R. H. Bahl, K. K. Nielsen, K. Engelbrecht, Experimental investigation of the effect of thermal hysteresis in the first order

material MnFe(P,As) applied in an AMR device, International Journal of Refrigeration 37 (2014) 303–306.

[13] V. K. Pecharsky, K. A. Gschneidner, Jr., Giant magnetocaloric effect in $Gd_5Si_2Ge_2$, Physical Reviews Letters 78 (1997) 4494–4497.

[14] H. Wada, Y. Tanabe, Giant magnetocaloric effect of $MnAs_{(1-x)}Sb_{(x)}$, Applied Physics Letters 79 (2001) 3302.

[15] O. Tegus, E. Brück, K. H. J. Buschow, F. R. de Boer, Transition-metal-based magnetic refrigerants for room-temperature applications, Nature 415 (2002) 150–152.

[16] A. Planes, L. Mañosa, M. Acet, Magnetocaloric effect and its relation to shape-memory properties in ferromagnetic Heusler alloys, Journal of Physics: Condensed Matter 21 (2009) 233201.

[17] S. Singh, L. Caron, S. W. D'Souza, T. Fichtner, G. Porcari, S. Fabbrici, C. Shekhar, S. Chadov, M. Solzi, C. Felser, Large magnetization and reversible magnetocaloric effect at the second-order magnetic transition in Heusler materials, Advanced Materials 28 (17) (2016) 3321–3325.

[18] A. Fujita, S. Fujieda, K. Fukamichi, H. Mitamura, T. Goto, Itinerant-electron metamagnetic transition and large magnetovolume effects in $La(Fe_xSi_{1-x})_{13}$ compounds, Physical Review B 65 (2001) 014410.

[19] R. Bjørk, C. R. H. Bahl, M. Katter, Magnetocaloric properties of $LaFe_{13-x-y}Co_xSi_y$ and commercial grade Gd, Journal of Magnetism and Magnetic Materials 322 (2010) 3882–3888.

[20] G. V. Brown, Magnetic heat pumping near room temperature, Journal of Applied Physics 47 (8) (1976) 3673–3680.

[21] J. A. Barclay, W. A. Steyert, Active magnetic regenerator, U.S. Patent No. 4,332,135 (1982).

[22] K. K. Nielsen, J. Tusek, K. Engelbrecht, S. Schopfer, A. Kitanovski, C. R. H. Bahl, A. Smith, N. Pryds, A. Poredos, Review on numerical modeling of active magnetic regenerators for room temperature applications, International Journal of Refrigeration 34 (2011) 603–616.

[23] M. Benedict, S. Sherif, M. Schroeder, D. Beers, The impact of magnetocaloric properties on refrigeration performance and machine design, International Journal of Refrigeration 74 (2017) 576–583.

[24] T. Lei, K. K. Nielsen, K. Engelbrecht, C. R. H. Bahl, H. Neves Bez, C. T. Veje, Sensitivity study of multi-layer active magnetic regenerators using first order magnetocaloric material $La(Fe,Mn,Si)_{13}H_y$, Journal of Applied Physics 118 (2015) 014903.

[25] C. Aprea, A. Greco, A. Maiorino, C. Masselli, A comparison between rare earth and transition metals working as magnetic materials in an AMR refrigerator in the room temperature range, Applied Thermal Engineering 91 (2015) 767–777.

[26] S. Jacobs, J. Auringer, A. Boeder, J. Chell, L. Komorowski, J. Leonard, S. Russek, C. Zimm, The performance of a large-scale rotary magnetic refrigerator, International Journal of Refrigeration 37 (2014) 84–91.

[27] U. Legait, F. Guillou, A. Kedous-Lebouc, V. Hardy, M. Almanza, An experimental comparison of four magnetocaloric regenerators using three different materials, International Journal of Refrigeration 37 (2014) 146–155.

[28] Y. Chiba, O. Sari, A. Smaili, C. Mahmed, P. Nikkola, Experimental Study of a Multilayer Active Magnetic Regenerator Refrigerator-Demonstrator, In: Dincer et al (Eds.) Progress in Clean Energy, Vol. 1, Springer International, Switzerland, 2015, Ch. 16, pp. 225–233.

[29] B. Pulko, J. Tušek, J. D. Moore, B. Weise, K. Skokov, O. Mityashkin, A. Kitanovski, C. Favero, P. Fajfarf, O. G. ajd Anja Waske, A. Poredoš, Epoxy-bonded La–Fe–Co–Si magnetocaloric plates, Journal of Magnetism and Magnetic Materials 375 (2015) 65–73.

[30] T. Lei, K. Navickaite, K. Engelbrecht, A. Barcza, H. Vieyra, K. K. Nielsen, C. R. H. Bahl, Passive characterization and active testing of epoxy bonded regenerators for room temperature magnetic refrigeration, Applied Thermal Engineering 128 (2018) 10–19.

[31] K. Navickaite, J. Liang, C. Bahl, S. Wieland, K. Engelbrecht, Experimental characterization of active magnetic regenerators constructed using laser beam melting technique, Applied Thermal Engineering 174 (2020) 115297.

[32] J. W. Conine, R. H. Hadley, Preparation of small solid pharmaceutical spheres, Drug and Ccosmetic Industry 106 (1970) 38–41.

[33] A. Barcza, M. Katter, V. Zellmann, S. Russek, S. Jacobs, C. Zimm, Stability and Magnetocaloric Properties of Sintered La(Fe, Mn, Si)$_{13}$H$_z$ Alloys, IEEE Transactions on Magnetics 47 (2011) 3391–3394.

[34] V. Basso, C. P. Sasso, M. Küpferling, A Peltier cells differential calorimeter with kinetic correction for the measurement of $c_p(H,T)$ and

$\Delta s(H,T)$ of magnetocaloric materials, Review of Scientific Instruments 81 (2010) 113904.

[35] V. Basso, M. Küpferling, C. Curcio, C. Bennati, A. Barzca, M. Katter, M. Bratko, E. Lovell, J. Turcaud, L. F. Cohen, Specific heat and entropy change at the first order phase transition of La(Fe-Mn-Si)13-H compounds, Journal of Applied Physics 118 (2015) 053907.

[36] E. Lovell, H. N. Bez, D. C. Boldrin, K. K. Nielsen, A. Smith, C. R. H. Bahl, L. F. Cohen, The $La(Fe,Mn,Si)_{13}H_z$ magnetic phase transition under pressure, Physica Status Solidi (RRL) - Rapid Research Letters 11 (2017) 1700143.

[37] H. N. Bez, K. K. Nielsen, A. Smith, C. R. H. Bahl, A detailed study of the hysteresis in $La_{0.67}Ca_{0.33}MnO_3$, Journal of Magnetism and Magnetic Materials 416 (2016) 429–433.

[38] Y.-Q. Li, F.-X. Hu, F.-R. Shen, K.-M. Qiao, J. Li, J. Wang, Y. Liu, J.-R. Sun, B.-G. Shen, Excellent mechanical properties and age stability of hydrogenated $La_{0.8}Ce_{0.2}Fe_{12.5}Mn_{0.2}Si_{1.3}H_\delta$ plates with extra Fe, Journal of Alloys and Compounds 743 (2018) 221–226.

[39] H. N. Bez, K. K. Nielsen, P. Norby, A. Smith, C. R. H. Bahl, Magnetoelastic coupling in $La(Fe,Mn,Si)_{13}H_y$ within the Bean-Rodbell model, AIP Advances 6 (2016) 056217.

[40] H. N. Bez, K. K. Nielsen, A. Smith, P. Norby, K. Ståhl, C. R. H. Bahl, Strain development during the phase transition of $La(Fe,Mn,Si)_{13}H_z$, Applied Physics Letters 109 (2016) 051902.

[41] G. F. Peixer, J. A. Lozano, J. R. Barbosa Jr., Performance evaluation of amrs using different casings, in: Book of Abstracts of the Danish Days on Caloric Materials and Devices (Poster Session), Roskilde, Denmark, 2017.

[42] P. V. Trevizoli, A. T. D. Nakashima, G. F. Peixer, J. R. Barbosa Jr., Performance evaluation of an active magnetic regenerator for cooling applications. Part I: experimental analysis and thermodynamic performance, International Journal of Refrigeration 72 (2016) 192–205.

[43] P. V. Trevizoli, A. T. Nakashima, J. R. Barbosa Jr., Performance evaluation of an active magnetic regenerator for cooling applications Part II: mathematical modeling and thermal losses, International Journal of Refrigeration 72 (2016) 206–217.

[44] S. Ergun, Fluid flow through packed collumn, Chemical engineering Progress 48 (1952) 89–94.

[45] F. Fortkamp, G. Lang, J. Lozano, J. Barbosa Jr., Numerical analysis of the influence of magnetic field waveforms on the performance of active magnetic regenerators, Journal of the Brazilian Society of Mechanical Sciences and Engineering 42 (2020) 378.

[46] M. Kaviany, Principles of Heat Transfer in Porous Media, 2nd Edition, Springer, 1995.

[47] D. L. Koch, J. F. Brady, Dispersion in fixed beds, Journal of Fluid Mechanics 154 (1985) 399–427.

[48] K. Engelbrecht, A numerical model of an active magnetic regenerator

refrigerator with experimental validation, Ph.D. dissertation, University of Wisconsin-Madison (2008).

[49] J. Pallares, F. X. Grau, A modification of a nusselt number correlation for forced convection in porous media, International Communications in Heat and Mass Transfer 37 (2010) 1187–1190.

[50] G. R. Hadley, Thermal conductivity of packed metal powders, International Journal of Heat and Mass Transfer 29 (1986) 909–920.

[51] C. H. Li, B. A. Finlayson, Heat transfer in packed beds - a reevaluation, Chemical Engineering Science 32 (1977) 1055–1066.

[52] P. Trevizoli, Development of thermal regenerators for magnetic cooling applications, D.Eng. dissertation, Federal University of Santa Catarina (2015).

[53] P. V. Trevizoli, J. R. Barbosa Jr., P. A. Oliveira, F. C. Canesin, R. T. S. Ferreira, Assessment of demagnetization phenomena in the performance of an active magnetic regenerator, International Journal of Refrigeration 35 (2012) 1043–1054.

[54] J. M. D. Coey, Magnetism and magnetic materials, Cambridge University Press, 2010.

[55] M. Sato, Y. Ishii, Simple and approximate expressions of demagnetizing factors of uniformly magnetized rectangular rod and cylinder, Journal of Applied Physics 66 (1989) 983–985.

[56] P. V. Trevizoli, J. A. Lozano, G. F. Peixer, J. R. Barbosa Jr., Design of nested halbach cylinder arrays for magnetic refrigeration applications, Journal of Magnetism and Magnetic Materials 395 (2015) 109–122.

[57] P. V. Trevizoli, A. T. D. Nakashima, G. F. Peixer, J. R. Barbosa Jr., Performance assessment of different porous matrix geometries for active magnetic regenerators, Applied Energy 187 (2017) 847–861.

[58] K. Navickaite, H. N. Bez, T. Lei, A. Barcza, H. Vieyra, C. R. Bahl, K. Engelbrecht, Experimental and numerical comparison of multi-layered $La(Fe,Si,Mn)_{13}H_y$ active magnetic regenerators, International Journal of Refrigeration 86 (2018) 322–330.